



# Postinfection treatment with a protease inhibitor increases survival of mice with a fatal SARS-CoV-2 infection

Chamandi S. Dampalla<sup>a,1</sup>, Jian Zheng<sup>b,1</sup>, Krishani Dinali Perera<sup>c</sup>, Lok-Yin Roy Wong<sup>b</sup>, David K. Meyerholz<sup>d</sup>, Harry Nhat Nguyen<sup>a</sup>, Maithri M. Kashipathy<sup>e</sup>, Kevin P. Battaile<sup>f</sup>, Scott Lovell<sup>g</sup>, Yunjeong Kim<sup>c,2</sup>, Stanley Perlman<sup>b,2</sup>, William C. Groutas<sup>a,2</sup>, and Kyeong-Ok Chang<sup>c,2</sup>

<sup>a</sup>Department of Chemistry, Wichita State University, Wichita, KS 67260; <sup>b</sup>Department of Microbiology and Immunology, The University of Iowa, Iowa City, IA 52242; <sup>c</sup>Department of Diagnostic Medicine and Pathobiology, College of Veterinary Medicine, Kansas State University, Manhattan, KS 66506; <sup>d</sup>Department of Pathology, The University of Iowa, Iowa City, IA 52242; <sup>e</sup>Protein Structure Laboratory, The University of Kansas, Lawrence, KS 66047; and <sup>f</sup>NYX, New York Structural Biology Center, Upton, NY 11973

Edited by Michael B. A. Oldstone, Scripps Research Institute, La Jolla, CA, and approved May 11, 2021 (received for review January 25, 2021)

Severe acute respiratory syndrome coronavirus 2 (SARS-CoV-2) infection continues to be a serious global public health threat. The 3C-like protease (3CLpro) is a virus protease encoded by SARS-CoV-2, which is essential for virus replication. We have previously reported a series of small-molecule 3CLpro inhibitors effective for inhibiting replication of human coronaviruses including SARS-CoV-2 in cell culture and in animal models. Here we generated a series of deuterated variants of a 3CLpro inhibitor, GC376, and evaluated the antiviral effect against SARS-CoV-2. The deuterated GC376 displayed potent inhibitory activity against SARS-CoV-2 in the enzyme- and the cell-based assays. The K18-hACE2 mice develop mild to lethal infection commensurate with SARS-CoV-2 challenge doses and were proposed as a model for efficacy testing of antiviral agents. We treated lethally infected mice with a deuterated derivative of GC376. Treatment of K18-hACE2 mice at 24 h postinfection with a derivative (compound 2) resulted in increased survival of mice compared to vehicle-treated mice. Lung virus titers were decreased, and histopathological changes were ameliorated in compound 2-treated mice compared to vehicle-treated mice. Structural investigation using high-resolution crystallography illuminated binding interactions of 3CLpro of SARS-CoV-2 and SARS-CoV with deuterated variants of GC376. Taken together, deuterated GC376 variants have excellent potential as antiviral agents against SARS-CoV-2.

SARS-CoV-2 | antiviral | protease inhibitors | K18-ACE2 mice

Coronaviruses are a large group of viruses that can cause a wide variety of diseases in humans and animals (1). They are single-stranded, positive-sense RNA viruses that belong to four genera, designated  $\alpha$ ,  $\beta$ ,  $\gamma$ , and  $\delta$  coronaviruses, in the *Coronaviridae* family (1). Human coronaviruses (229E, NL63, OC43, and HKU1) generally cause mild upper respiratory infections. However, global outbreaks of new human coronavirus infections with severe respiratory disease have periodically emerged from animals, including severe acute respiratory syndrome coronavirus (SARS-CoV), Middle East respiratory syndrome coronavirus (MERS-CoV) and, most recently, severe acute respiratory syndrome coronavirus 2 (SARS-CoV-2), the causative agent of COVID-19 (2). SARS-CoV-2 emerged in China in December 2019 and subsequently spread throughout the world. Ominously, the diversity of coronavirus strains in potential animal reservoirs suggests that emerging and reemerging pathogenic coronaviruses will continue to pose a significant threat to public health. Currently, vaccines using different platforms have been developed or under development, and three vaccines just became available in the United States for COVID-19 licensed for emergency use, with more others expected to be available soon. The specific therapeutic interventions that are currently licensed or given emergency use authorizations include remdesivir (Veklury), a combination of remdesivir and a JAK inhibitor, baricitinib, and

a single monoclonal antibody or a mixture of monoclonal antibodies.

Although additional clinical trial results will be needed to fully understand the efficacy of these treatments, the currently available clinical data on these treatments showed limited effects of these treatments in reducing disease progression or facilitating recovery (3). Clinical presentation of COVID-19 patients varies from being asymptomatic to several respiratory disease that may lead to death. Viral replication in the respiratory tract peaks during the first week of infection and decline, and in severe COVID-19 cases extensive inflammatory responses in the lungs initiated by viral replication dominate in the late stage, being the main culprit for lethality (4). Therefore, a combination of antiviral agents and immune modulators such as dexamethasone has been suggested to

## Significance

Protease inhibitors targeting viral 3C-like protease are attractive therapeutic options for COVID-19. Here, we synthesized deuterated variants of a coronavirus protease inhibitor, GC376, and determined the therapeutic efficacy in a lethal mouse model. The transgenic mice infected with severe acute respiratory syndrome coronavirus 2 (SARS-CoV-2), a causative agent of COVID-19, develop lung pathology resembling that of severe COVID-19 patients and were used for antiviral drug testing. The deuterated variants of GC376 have improved potency against SARS-CoV-2 in *in vitro* assays. Furthermore, treatment with a deuterated variant starting at 24 h postinfection resulted in significantly increased survival of mice compared to vehicle-treated mice. The results suggest that deuterated variants have excellent potential as antiviral agents against SARS-CoV-2.

Author contributions: Y.K., S.P., W.C.G., and K.-O.C. designed research; C.S.D., J.Z., K.D.P., L.-Y.R.W., H.N.N., M.M.K., S.L., and Y.K. performed research; D.K.M., K.P.B., S.L., Y.K., S.P., W.C.G., and K.-O.C. analyzed data; and S.L., Y.K., S.P., W.C.G., and K.-O.C. wrote the paper.

Competing interest statement: Kansas State University, Wichita State University, and The University of Iowa have jointly filed a provisional patent application covering compound 1-11 as well as related compounds, with K.-O.C., Y.K., S.P., and W.C.G. as inventors. Title: Improvement of efficacy and pharmacokinetics of protease inhibitors via deuteration (application 63036542). No author is involved in consulting regarding this study.

This article is a PNAS Direct Submission.

This open access article is distributed under [Creative Commons Attribution License 4.0 \(CC BY\)](https://creativecommons.org/licenses/by/4.0/).

<sup>1</sup>C.S.D. and J.Z. contributed equally to this work.

<sup>2</sup>To whom correspondence may be addressed. Email: ykim@ksu.edu, stanley-perlman@uiowa.edu, bill.groutas@wichita.edu, or kchang@vet.ksu.edu.

This article contains supporting information online at <https://www.pnas.org/lookup/suppl/doi:10.1073/pnas.2101555118/-DCSupplemental>.

Published July 1, 2021.

improve clinical outcome in advanced diseases (3). Currently, only the nucleoside analog remdesivir is available for COVID-19 patients as a Food and Drug Administration (FDA)-approved drug, and additional potent direct-acting antiviral agents, such as protease inhibitors, are urgently required to enrich the drug arsenal against SARS-CoV-2 infection.

The SARS-CoV-2 genome encodes two polyproteins which are processed by a 3C-like protease (3CLpro) and a papain-like protease. These viral proteases are essential for viral replication, making them attractive targets for drug development (5–7). It is furthermore acknowledged that, in addition to the development of effective vaccines, the concurrent identification of FDA-approved drugs that can be repurposed for use against SARS-CoV-2 may accelerate the development and implementation of effective countermeasures against the virus (reviewed in ref. 8). We previously described a series of 3CLpro inhibitors (including GC376) with activities against multiple coronaviruses, including SARS-CoV (9), MERS-CoV (6, 10), and SARS-CoV-2 (10). GC376 was recently demonstrated in clinical trials to have efficacy against a fatal feline coronavirus infection, feline infectious peritonitis (FIP) (11, 12), and is currently in clinical development for treating FIP in cats.

Some mice that express human ACE2 or hamsters develop weight loss and lung histopathology but they have no or little mortality following human SARS-CoV-2 infection (13–15). Thus, they serve as good models for asymptomatic, mild, and moderate SARS-CoV-2 infection and for studies of viral transmission. Currently only a few fatal infection animal models are available that can recapitulate the key features of severe pathogenesis in humans with COVID-19. Transgenic hACE2-HFH4 mice (16) and K18-hACE2 mice (17–19), which express human angiotensin I-converting enzyme 2 (ACE2) receptor under HFH4 or K18 promoter, or a mouse-adapted SARS-CoV-2 MA10 strain (7) can lead to fatality dependent upon virus challenge doses. Neural invasion of the brain variably occurs in hACE2 transgenic mice and is associated with a fatal outcome. In the absence of brain infection, however, the respiratory infection is still lethal, depending on initial virus inoculum. Although there is evidence of neurological complications, such as encephalopathy and encephalitis, in COVID-19 patients (20), the relevance of brain infection in these animal models in human neurological disease needs further clarification. The fatal infection models are useful models for efficacy testing of antiviral agents as they show viral replication in the lungs with inflammation and virus-induced histopathological changes that resemble severe COVID-19 infection in humans. In the K18-hACE2 model, pre- and postinfection treatment efficacy of human convalescent plasma from a recovered COVID-19 patient was previously studied (18), and antiviral agents such as GC376 (7, 21) were tested. We report herein the results of our studies related to the synthesis and evaluation of deuterated GC376 variants which have enhanced antiviral activity and display efficacy in a fatal mouse model (K18-hACE2 mice) of SARS-CoV-2.

## Results

**Deuterated Variants of GC376 Display Potent Inhibitory Activity against SARS-CoV-2 in the Enzyme- and the Cell-Based Assays.** We synthesized deuterated variants based on GC376 (SI Appendix and SI Appendix, Fig. S1) and compared their inhibitory activities against SARS-CoV-2 to nondeuterated GC376 in the enzyme- and the cell-based assays (Table 1). Three different variants of deuterated aldehyde compounds (compounds 1, 6, and 9 with R<sub>1</sub>, R<sub>2</sub>, and R<sub>3</sub>, respectively) as well as their bisulfite adducts (compounds 2, 7, and 10) were prepared for the testing. In addition, an  $\alpha$ -ketoamide (compound 5) based on compound 1 and prodrug variations (compounds 3, 4, 8, and 11) of the bisulfite adducts of aldehydes (compounds 1, 6, and 9) were synthesized for the testing. In the enzyme assay, the bisulfite adducts showed 50% inhibitory concentration (IC<sub>50</sub>) values similar to their aldehyde counterparts

**Table 1. Structures and inhibitory activities of deuterated variants of GC376 against SARS-CoV-2 in the enzyme and cell-based assays**

Compound	IC <sub>50</sub> , $\mu$ M	SARS-CoV-2		
		EC <sub>50</sub> , $\mu$ M		CC <sub>50</sub> , $\mu$ M
		Vero E6	A549-ACE2	
1	0.17 $\pm$ 0.05	0.068 $\pm$ 0.01	0.086 $\pm$ 0.01	>100
2	0.18 $\pm$ 0.04	0.086 $\pm$ 0.02	0.069 $\pm$ 0.01	>100
3	0.71 $\pm$ 0.06	N/D*	N/D	>100
4	0.80 $\pm$ 0.1	N/D	N/D	>100
5	1.31 $\pm$ 0.55	N/D	N/D	>100
6	0.16 $\pm$ 0.03	0.077 $\pm$ 0.01	0.075 $\pm$ 0.01	>100
7	0.19 $\pm$ 0.04	0.079 $\pm$ 0.01	0.10 $\pm$ 0.01	>100
8	0.68 $\pm$ 0.35	N/D	N/D	>100
9	0.24 $\pm$ 0.01	N/D	N/D	>100
10	0.21 $\pm$ 0.02	N/D	N/D	>100
11	0.77 $\pm$ 0.12	N/D	N/D	>100
GC376	0.41 $\pm$ 0.07	0.23 $\pm$ 0.01	N/D	>100

(A) R<sub>1</sub>, R<sub>2</sub> and R<sub>3</sub> deuterated moieties. (B) Structures of deuterated variants. (C) The activity and cytotoxicity of deuterated variants of GC376. IC<sub>50</sub>, the 50% inhibitory concentration determined in the enzyme assay; EC<sub>50</sub>, the 50% effective concentration determined in Vero E6 cells; and CC<sub>50</sub>, the 50% cytotoxic concentration determined in Vero E6 and CRFK cells. The values indicate the means and the SDs of the means. N/D: not determined.

(Table 1, structure C). The  $\alpha$ -ketoamide derivative (compound 5) of compound 1 had markedly decreased potency in the enzyme assay. Likewise, prodrug counterparts (compounds 3, 4, 8, and 11) have significantly increased IC<sub>50</sub> values compared to their aldehyde and bisulfite precursors (Table 1, structure C). The deuterated compounds that were more effective than GC376 in the enzyme assay were tested in the cell-based assay using Vero E6 and A549-ACE2 cell lines. The 50% effective concentration (EC<sub>50</sub>) values of the tested deuterated compounds (compounds 1, 2, 6, and 7) (0.068 to 0.086  $\mu$ M) were comparable in those cell lines and lower than GC376 by 2.67–3.38-fold in Vero E6 cells. All compounds, including GC376, did not show any cytotoxicity up to 100  $\mu$ M (Table 1, structure C).

**Structures of 3CLpro of SARS-CoV and SARS-CoV-2 Bound with Deuterated Variants of GC376.** Compound 2 with a bisulfite adduct warhead and compound 5 with  $\alpha$ -ketoamide were cocrystallized with the 3CLpro of SARS-CoV-2 and SARS-CoV and examined by X-ray crystallography. Examination of the active site of SARS-CoV-2 3CLpro revealed the presence of prominent difference electron density consistent with compound 2 covalently bound to the S $\gamma$  atom of Cys<sup>145</sup> in each subunit (Fig. 1 A and B). Interestingly, the electron density was most consistent with the S-enantiomer at the newly formed stereocenter. Although the electron density in subunit B did contain a small “bulge” that may be due to the R-enantiomer, only one configuration was modeled. Compound 2 adopts the same binding mode in each subunit and forms identical hydrogen bond interactions with residues Phe<sup>140</sup>,

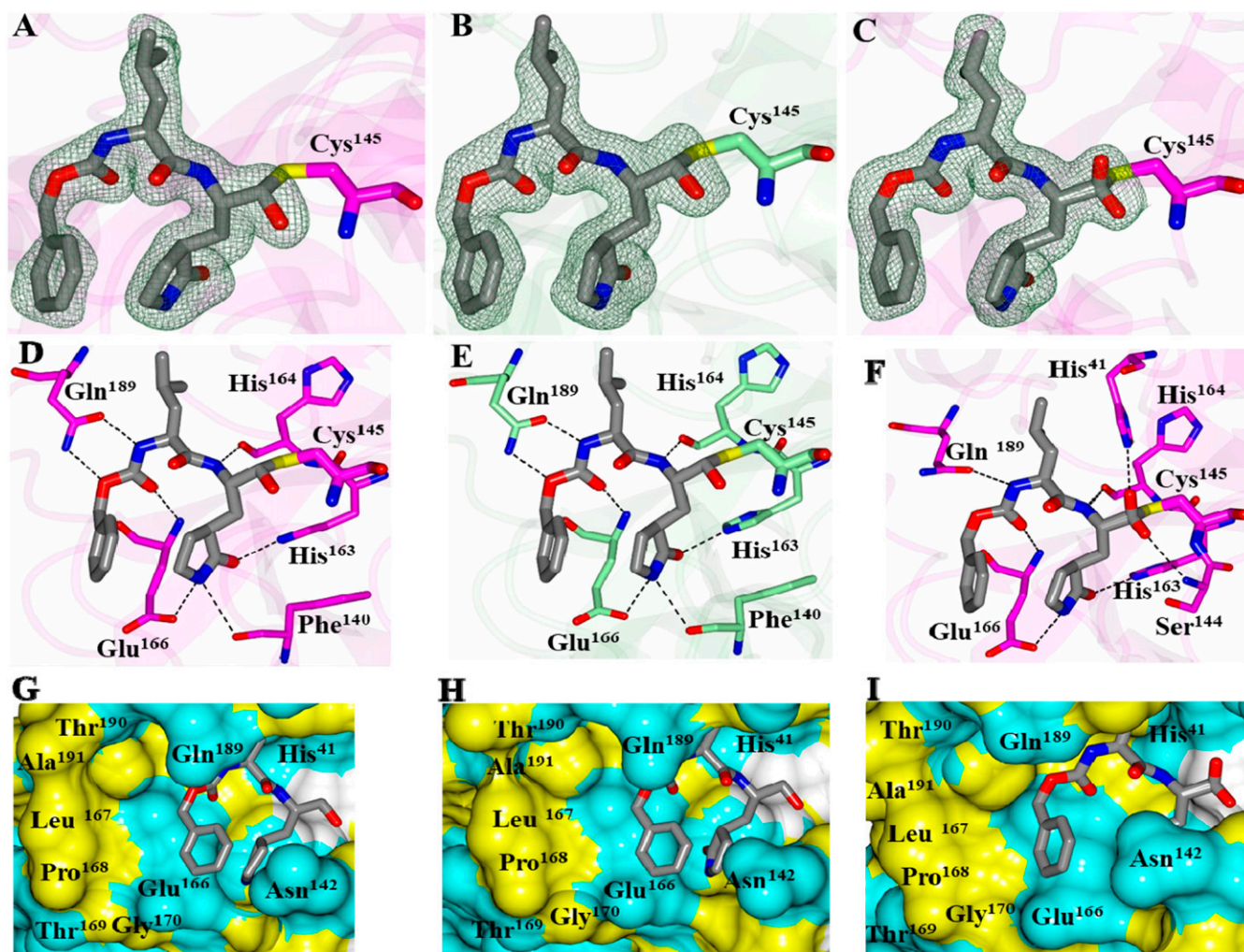


**Fig. 1.** Cocystal structures of SARS-CoV-2 3CLpro (A, D, G: subunit A and B, E, H: subunit B) and SARS-CoV 3CLpro (C, F, and I) in complex with compound 2. A–C show  $F_o - F_c$  omit maps (green mesh) contoured at  $3\sigma$ . D–F show hydrogen bond interactions (dashed lines) between the inhibitor and the 3CL protease. G–I show electrostatic surface representation of the binding pocket occupied by the inhibitor. Neighboring residues are colored yellow (nonpolar), cyan (polar), and white (weakly polar).

His<sup>163</sup>, His<sup>164</sup>, Glu<sup>166</sup>, and Gln<sup>189</sup> (Fig. 1 D and E). As we generally observed in studies of SARS-CoV 3CLpro, the electron density map was consistent with both the R- and S-enantiomers of compound 2 at the new stereocenter formed by covalent attachment of the S<sub>γ</sub> atom of Cys<sup>145</sup> in the cocystal structure of SARS-CoV 3CLpro (Fig. 1C). Overall, the hydrogen bond interactions are nearly identical relative to SARS-CoV-2 3CLpro. The main difference is that a hydrogen bond is formed between His<sup>41</sup> and the hydroxyl of compound 2 in the R-enantiomer and a long contact (3.29 Å) to the backbone N-atom of Ser<sup>144</sup> with the hydroxyl of the S-enantiomer (Fig. 1F). Notably, the hydroxyl in compound 2 bound to SARS-CoV-2 3CLpro is 3.38 Å and 3.39 Å from the N-atom of Ser<sup>144</sup>, which would be a weak hydrogen bond contact. The benzyl ring in both structures is positioned outward from the hydrophobic S<sub>4</sub> subsite and is directed toward the surface as shown in Fig. 1 G–I. Notably, the structures of SARS-CoV-2 3CLpro in complex with nondeuterated G376 and its precursor aldehyde GC373 (Protein Data Bank [PDB] ID codes 6WTJ and 6WTK, respectively) adopt the same binding mode as that observed for compound 2 (SI Appendix, Fig. S2). Superposition yielded rmsd of 0.59 Å (GC376) and 0.55 Å (GC373) between C $\alpha$  atoms for 299 residues aligned (22).

The structures of SARS-CoV and SARS-CoV-2 3CLpro in complex with compound 5 also contained prominent difference in electron density consistent with the inhibitor covalently bound to the S<sub>γ</sub> atom of Cys<sup>145</sup> (SI Appendix, Fig. S3 A and D). The entire inhibitor could be modeled in subunit A but was partially disordered in subunit B and the benzyl group in the S<sub>4</sub> subsite could not be modeled for SARS-CoV. The inhibitor forms direct hydrogen bond interactions similar to compound 2, as shown in SI Appendix, Fig. S3 B and E. The benzyl group in subunit A of both SARS-CoV and SARS-CoV-2 3CLpro is positioned near hydrophobic residues within the S<sub>4</sub> subsite (SI Appendix, Fig. S3 C and F). The benzyl ring in the  $\alpha$ -ketoamide region of the inhibitor is positioned near a cleft formed by Asn<sup>142</sup>/Gly<sup>143</sup> in both structures. Interestingly, the compound bound to subunit B of SARS-CoV-2 3CLpro adopts a conformation similar to that observed for compound 2 in which the benzyl group is directed away from the S<sub>4</sub> subsite and toward the surface (SI Appendix, Fig. S4). Therefore, it appears the structure of SARS-CoV-2 3CLpro in complex with compound 5 serendipitously contains two binding modes of the inhibitor.

**Treatment with Compound 2 at 24 h after SARS-CoV-2 Infection Demonstrates Efficacy against Fatal SARS-CoV-2 Infection in K18-hACE2 Mice.** Compound 2 was tested in SARS-CoV-2-infected K18-hACE2 mice for protective efficacy, because it potently inhibited

SARS-CoV-2 in the cell-based assay described above. The dose curve of compound 2 against SARS-CoV-2 in cell culture is shown in Fig. 2A. In the first experiment, infection with  $2 \times 10^3$  plaque-forming units (pfu) per mouse led to body weight loss in all vehicle-treated mice, resulting in 50% survival by 9 d postinfection (dpi) (Fig. 2B). Mice treated with compound 2 ( $100 \text{ mg}\cdot\text{kg}^{-1}\cdot\text{d}^{-1}$ , once a day) starting from 24 h postinfection (1 dpi) lost body weight, but loss was less severe compared to vehicle-treated mice with statistically significant differences ( $0.002 < P < 0.049$ ) on most days between 5 and 10 dpi (Fig. 2C). All compound 2-treated mice gradually gained body weight and were alive at the end of the study (15 dpi) (Fig. 2C), although survival of these mice was not statistically different ( $P = 0.18$ ) compared to vehicle-treated mice, likely due to lower fatality of control mice. In the second and third experiment, a higher virus challenge dose ( $5 \times 10^3$  pfu per mouse) was given before treatment with vehicle or compound 2 ( $125 \text{ mg}\cdot\text{kg}^{-1}\cdot\text{d}^{-1}$ , once a day) started 24 h postinfection. In the second experiment, the vehicle-treated mice exhibited greater body weight loss than those with the lower virus challenge (experiment 1), and none of the mice ( $n = 4$ ) survived past 7 dpi (Fig. 2D). Weight losses of mice treated with compound 2 were significantly less than those with vehicle treatment at 3, 5, and 6 dpi ( $0.009 < P < 0.017$ ), and compound 2-treated mice started to gain weight from 10 dpi (Fig. 2E). In contrast to 0% survival in vehicle-treated mice, five out of six compound 2-treated mice (83%) survived at the end of the study (15 dpi), resulting in significant improved survival of compound 2-treated mice ( $P = 0.011$ ). In the third experiment, although the vehicle- or compound 2-treated mice did not show a statistically difference in body weight loss for 0 to 5 dpi, compound 2-treated mice started gaining weight from 6 to 7 dpi (Fig. 2F). All compound 2-treated mice survived at the end of the study (15 dpi), while all vehicle-treated mice died by 5 dpi ( $P = 0.0084$ ).

**Treating Infected K18 hACE2 Mice with Compound 2 Reduces Viral Titers and Histopathological Changes in the Lungs.** In two separate experiments, mice were infected with  $5 \times 10^3$  pfu SARS-CoV-2 virus and treated with compound 2 or vehicle starting from 1 dpi (24 h postinfection). In both experiments, lung virus titers peaked at 2 dpi and decreased at 5 dpi in both groups. Virus titers were statistically lower in compound 2-treated mice compared to vehicle-treated mice at 5 dpi by  $\sim 10.54$ - to  $13.57$ -fold in both experiments ( $P = 0.0028$  and  $0.004$ , respectively) (Fig. 3A and B), although a statistically significant reduction of virus titers was also observed only at 2 dpi in the second experiment ( $P = 0.004$ ) (Fig. 3B). Lung pathology in vehicle-treated mice obtained from the first experiment included diffuse alveolar damage with progressive alveolar or interstitial lesions characterized by edema, inflammation, and focal cytomegaly in some alveolar lining cells. Additional features include an accumulation of immune effector cells, including granulocytes and macrophages, evidence of cell death, hemorrhage, hyaline membranes, and occasional vascular thrombi. Histopathological observations were in agreement with improved survival observed in SARS-CoV-2-infected animals treated with compound 2 (Fig. 3C). At 2 dpi, alveolar edema was seen in some lung tissue sections (average score 0.5) in the lungs from animals treated with vehicle (Fig. 3C, a and b), but there were few lesions in the lungs from compound 2-treated animals (average score 0) (Fig. 3C, c and d). Mild perivascular infiltrates were seen in lungs from both vehicle- and compound 2-treated animals at 2 dpi (Fig. 3C, a-d). At 5 dpi, while severe edema (average score 4) and perivascular infiltrates (average score 3.5) were evident in the lungs from vehicle-treated animals (Fig. 3C, e and f), mild edema (average score 2) and perivascular infiltrations (average score 2) were observed in the lungs of compound 2-treated animals (Fig. 3C, g and h). K18-hACE2 mice infected with SARS-CoV-2 sometimes develop encephalitis. Low levels of virus (340, 1,660, and 660 pfu per brain) but no pathological changes

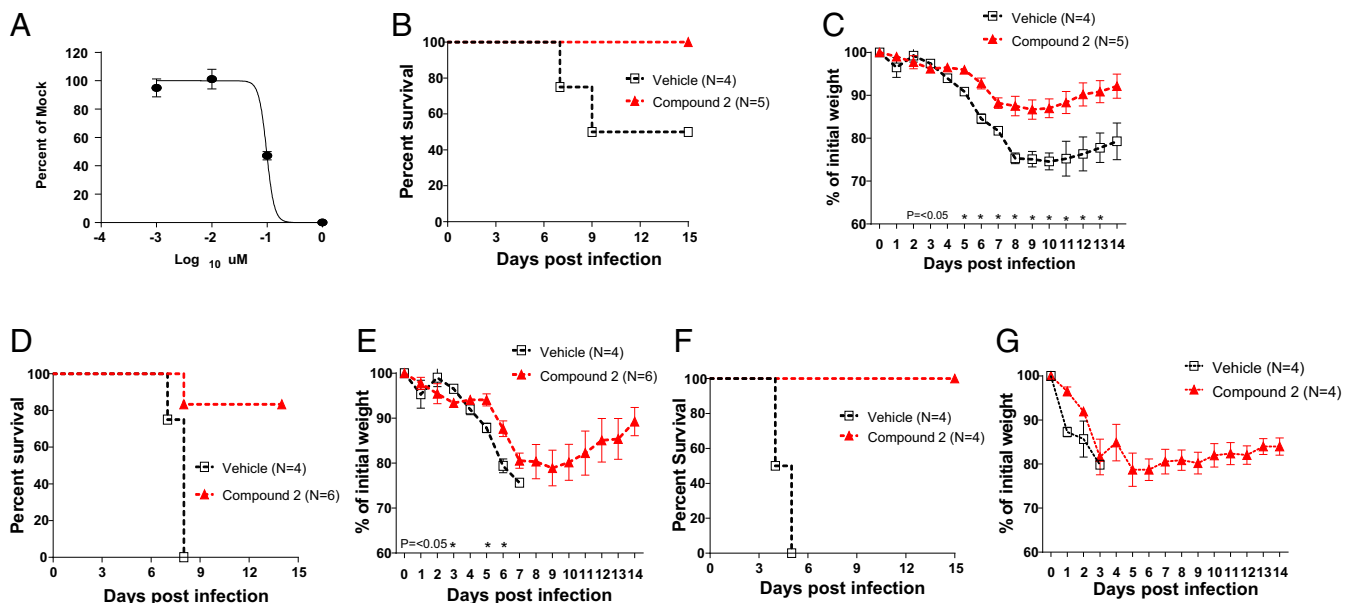


**Fig. 2.** Therapeutic treatment of K18-hACE2 mice infected with SARS-CoV-2. (A) A dose-dependent curve for compound 2 against SARS-CoV-2 in cell culture. Confluent Vero E6 cells were inoculated with SARS-CoV-2, and medium containing various concentrations of compound 2 and agar was applied to the cells. After 48 to 72 h, plaques in each well were counted, and  $EC_{50}$  values were determined by GraphPad Prism software. (B and C) The K18-hACE2 mice infected with SARS-CoV-2 with  $2 \times 10^3$  pfu per mouse were treated with compound 2 at  $100 \text{ mg}/\text{kg}$  once per day or vehicle starting at 1 dpi for up to 10 d, and survival (B) and weight (C) were monitored for 15 d. (D–F) In two separate experiments, the K18-hACE2 mice infected with SARS-CoV-2 with  $5 \times 10^3$  pfu/mouse were treated with compound 2 at  $125 \text{ mg}/\text{kg}$  once per day or vehicle starting at 1 dpi for up to 10 d, and survival (D and G) and weight (E and F) were monitored for 15 d. The data points represent the means and the SDs of the means. The analysis of survival curves between groups was performed using a log-rank (Mantel–Cox) test in GraphPad Prism software. The symbols and the bars in C and E represent the means and the SDs of the means. Asterisks indicate statistical difference between vehicle and compound 2-treated groups determined using multiple t tests in GraphPad Prism software ( $P < 0.05$ ).

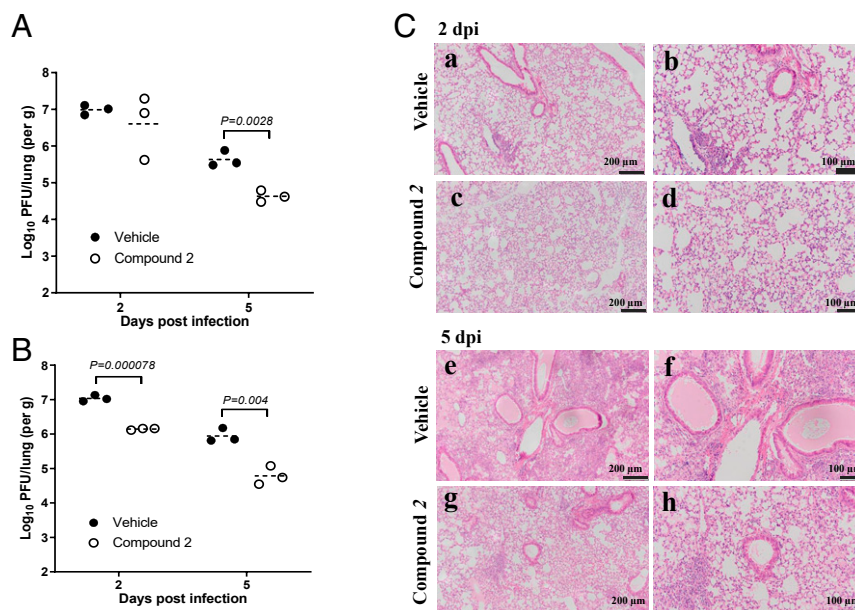


**Fig. 3.** Lung virus titers and histopathology of K18-hACE2 mice infected with SARS-CoV-2 and treated with vehicle or compound 2 starting at 1 dpi. The lungs and the brains were collected at 2 and 5 dpi for virus titration (A and B) and histopathology (C). (A and B) Lung virus load in vehicle- or compound 2–treated groups in two separate experiments. Each symbol represents an individual mouse, and the dashed line represents the means and the dotted line is the limit of detection (200 pfu). Confluent Vero E6 cells were inoculated with serial dilutions of lung homogenates and agar was applied to the cells. After 48 to 72 h, plaques in each well were counted and pfu per gram was calculated. Statistical significance was determined using multiple *t* tests in GraphPad Prism software ( $P < 0.05$ ). (C) Lungs were examined for edema and for hyaline membrane formation. Lung sections were stained with hematoxylin and eosin for histopathology at 2 (a to d) or 5 dpi (e to h). Histopathology images are shown at either 10X (a, c, e, and g) or 20X (b, d, f, and h) for vehicle control (a, b, e, and f) and compound 2–treated groups (c, d, g, and h).

were detected in vehicle-treated mice. In contrast, neither pathological changes nor infectious virus was detected at 2 and 5 dpi in the brains of mice treated with compound 2 (detection limit: 200 pfu per gram).

## Discussion

The advent of SARS-CoV-2, the causative agent of COVID-19, has provided the impetus behind worldwide efforts to develop effective countermeasures against the virus for the treatment of COVID-19, including the use of repurposed drugs (reviewed in refs. 23 and 24). Indeed, remdesivir, a nucleoside analog which was originally developed and FDA-approved for treating Ebola virus infection, has been shown to be a potent inhibitor of SARS-CoV-2 (25–27) and recently approved for COVID-19. However, effects in patients have been modest, with some studies showing no efficacy (28–31). Multiple FDA-approved drugs which exert their antiviral effects by impeding key steps in the viral lifecycle, including virus entry and fusion and viral replication, among others, are currently under intense investigation for use against SARS-CoV-2 (23, 24, 32–34). Efforts in developing small-molecule inhibitors targeting the virus proteases of SARS-CoV-2 have focused on blocking 3CLpro (35–37). Recently, GC376, a 3CL protease inhibitor under commercial development for FIP, was reported to have anti-SARS-CoV-2 activity by us (6) and other groups (22, 38, 39), which suggests this compound is a lead compound for COVID-19 amenable to further optimization. The *in vitro* antiviral effects of GC376 are comparable to other remdesivir and other nucleoside analogs and protease inhibitors under development against SARS-CoV-2 (38, 40–42). The antiviral compounds, including GC376, showed antiviral effects against SARS-CoV-2 in human ACE2–expressing transgenic mice (27, 40, 43) or in rhesus macaques (25) with nonlethal infection. However, few reports are available on the effects of these compounds in animal models with lethal infection. In a report where GC376 was given 3 h after virus

inoculation that led to 100% fatality there was no difference in survival of K18 mice, although reduced viral load and inflammation was observed in the lungs compared to vehicle-treated controls (7).

Based on the multiple potential advantages frequently accrued from the introduction of deuterium in a drug, such as improved pharmacokinetics, reduction in toxicity, and enhanced potency (reviewed in ref. 44), it was envisaged that deuterated variants of GC376 could function as therapeutics with superior characteristics compared to the corresponding nondeuterated GC376 drug. Deuterated small compounds contain one or more deuterium, a heavier nonradioactive isotope of hydrogen, as a chemical element in place of hydrogen. Higher mass of deuterium makes carbon–deuterium bonds more resistant to oxidative degradation, and thus the deuterization approach has been utilized in medicinal chemistry to enhance drug property, and at least one deuterated drug has been licensed with others in development (44). Therefore, we generated three deuterated variants of GC376 by replacing hydrogen with deuterium at the metabolic soft spots encompassed in the R-site (aromatic ring and benzylic carbon) and evaluated their activity in the enzyme- and the cell-based assays. All three R-site–deuterated variants (aldehydes and their bisulfite adducts) showed modestly increased potency compared to GC376, which was more apparent in the cell-based assays than in the enzyme assay (Table 1, structure C).

Crystal structures of deuterated GC376 (compound 2) and the 3CLpro of SARS-CoV-2 revealed that deuteration did not alter the interactions between GC376 and 3CLpro which are reported by other groups (22, 39, 45). It may be speculated that the enhanced activity of the deuterated compounds can be attributed to tighter binding to the target, which was observed with other deuterated compounds (44), or improved physicochemical properties of the compound. However, further study is needed to understand the mechanism. Substitution of the aldehyde warhead in compound 1 with an  $\alpha$ -ketoamide (compound 5) significantly

decreased potency, which confirms earlier findings by us (9, 46) that ketoamide is less suitable for coronavirus 3CLpro inhibition. Employing an OCOMethyl or n-pentyl ester derivative of bisulfite adducts to produce prodrug variants (compounds **3**, **4**, **8**, and **11**) led to reduced potency in the enzyme assay, which may be due to inefficient conversion to the active compound in the enzyme assay.

In the K18-hACE2 mice infected with SARS-CoV-2, once daily administration of compound **2** starting at 24 h postinfection to mice infected with 50% or 100% lethality resulted in significant reductions in body weight loss and nearly complete survival of K18 mice. The kinetics of virus clearance was enhanced and lung pathological changes were diminished by drug treatment.

In summary, we show that deuterated variants of GC376 are potent inhibitors of SARS-CoV-2 replication and significantly enhance survival of infected mice. Importantly, this approach has wide applicability, and strategic deuteration can be extended to multiple FDA-approved drugs currently under investigation as COVID-19 therapeutics with potential improvement in clinical outcomes.

## Materials and Methods

**Study Design.** The primary objective of this study was to evaluate the antiviral activity of deuterated variants of GC376, a protease inhibitor that is currently under investigation for the treatment of FIP and COVID-19, against SARS-CoV-2 *in vitro*, as well as antiviral efficacy in a fatal mouse model of SARS-CoV-2 infection.

**Biocontainment and Biosafety of Coronaviruses.** All studies with SARS-CoV-2 were performed in biosafety level 3 facilities at The University of Iowa. All experiments were conducted under protocols approved by the Institutional Biosafety Committee at the University of Iowa according to guidelines set by the Biosafety in Microbiological and Biomedical Laboratories, the US Department of Health and Human Services, the US Public Health Service, the US Centers for Disease Control and Prevention, and the National Institutes of Health.

**Synthesis of Deuterated Variants of GC376 3CLpro Inhibitors.** Compounds **1** through **11** were readily synthesized using a reaction sequence similar to the one previously reported by us (*SI Appendix, Fig. S1*) (47–49) and are listed in Table 1, structure B. Briefly, the deuterated alcohol inputs (Table 1, structure A) were reacted with (L) leucine isocyanate methyl ester to yield the corresponding dipeptidyl methyl esters which were then hydrolyzed to the corresponding acids with lithium hydroxide in aqueous tetrahydrofuran. Subsequent carbonyl dimidazole-mediated coupling of the acids to glutamine surrogate methyl ester (**50**) furnished the dipeptidyl methyl esters. Lithium borohydride reduction yielded the alcohols which were then oxidized to the corresponding aldehydes with Dess–Martin periodinane reagent. The bisulfite adducts were generated by treatment with sodium bisulfite in aqueous ethanol and ethyl acetate (**51**). An alternative convergent synthesis of compounds **1** through **11** entailed the activation of a deuterated alcohol with disuccinimidoyl carbonate followed by sequential coupling with a dipeptidyl amino alcohol and oxidation with Dess–Martin periodinane. The synthesis of  $\alpha$ -ketoamide compound **5** was accomplished by reacting the Z-protected dipeptidyl aldehyde with benzyl isonitrile to yield the  $\alpha$ -hydroxyketoamide followed by Dess–Martin oxidation. Prodrug compounds **3**, **4**, **8**, and **11** were synthesized by refluxing the aldehyde bisulfite adduct with acetic anhydride or n-hexanoic anhydride (**49**).

**Fluorescence Resonance Energy Transfer (FRET) Enzyme Assay.** The cloning, expression, and purification of the 3CLpro of SARS-CoV-2 were conducted by a standard method described previously (6). The codon-optimized complementary DNA of full-length 3CLpro of SARS-CoV-2 (GenBank accession number MN908947.3) fused with sequences encoding 6 histidine at the N terminal was synthesized by Integrated DNA Technologies. The synthesized gene was subcloned into the pET-28a (+) vector. The FRET enzyme assays were conducted as described previously (35). Briefly, stock solutions of compounds **1** through **11** were prepared in dimethyl sulfoxide (DMSO) and diluted in assay buffer, which was composed of 20 mM Hepes buffer, pH 8, containing NaCl (200 mM), ethylenediaminetetraacetic acid (0.4 mM), glycerol (60%), and 6 mM dithiothreitol. The SARS-CoV-2 3CL protease was mixed with serial dilutions of each compound or with DMSO in 25  $\mu$ L of assay buffer and incubated at room temperature for 1 h (SARS-CoV-2 and SARS-CoV), followed by the addition of 25  $\mu$ L of assay buffer containing substrate (FAM-SAVLQ/SG-QXL520; AnaSpec). The substrate was derived from the cleavage sites on the viral polyproteins of SARS-CoV. Fluorescence readings were obtained using an excitation wavelength of 480 nm

and an emission wavelength of 520 nm on a fluorescence microplate reader (FLx800; Biotec) at 1 h following the addition of the substrate. Relative fluorescence units were determined by subtracting background values (substrate-containing well without protease) from the raw fluorescence values, as described previously (6). The dose-dependent FRET inhibition curves were fitted with a variable slope using GraphPad Prism software to determine the IC<sub>50</sub> values of the compounds, which are listed in Table 1, structure C.

**Cell-Based Assay for Antiviral Activity.** Compounds **1**, **2**, **6**, and **7** were investigated for their antiviral activity against the replication of SARS-CoV-2. Briefly, confluent Vero E6 cells were inoculated with SARS-CoV-2 at 50 to 100 pfu per well, and medium containing various concentrations of each compound and agar was applied to the cells. After 48 to 72 h, plaques in each well were counted. The EC<sub>50</sub> values were determined by GraphPad Prism software using a variable slope (6).

**Nonspecific Cytotoxic Effects.** The 50% cytotoxic concentrations (CC<sub>50</sub>) of compounds **1** through **11** were determined in Vero E6 and CRFK cells. Confluent cells grown in 96-well plates were incubated with various concentrations (1 to 100  $\mu$ M) of each compound for 72 h. Cell cytotoxicity was measured by a CytoTox 96 nonradioactive cytotoxicity assay kit (Promega), and the CC<sub>50</sub> values were calculated using a variable slope by GraphPad Prism software (Table 1, structure C).

**X-Ray Crystallographic Studies: Protein Purification, Crystallization, and Data Collection.** Purified SARS-CoV 3CLpro and SARS-CoV-2 (**6**) 3CLpro were concentrated to 22.0 mg/mL (0.64 mM) and 9.6 mg/mL (0.28 mM), respectively, in 100 mM NaCl, 20 mM Tris, pH 8.0, for crystallization screening. All crystallization experiments were set up using an NT8 drop-setting robot (Formulatrix Inc.) and UVXPO MRC (Molecular Dimensions) sitting-drop vapor-diffusion plates at 18 °C. One hundred nanoliters of protein and 100 nL crystallization solution were dispensed and equilibrated against 50  $\mu$ L of the latter. Stock solutions of compounds **2** and **5** (100 mM) were prepared in DMSO and the 3CLpro:inhibitor complexes were prepared by adding 2 mM ligand to the proteases and incubating on ice for 1 h. Crystals were obtained in 1 to 2 d from the following conditions. SARS-CoV 3CLpro complex with compound **2**: Index HT screen (Hampton Research) condition H4 (30% [wt/vol] polyethylene glycol [PEG] 3350, 200 mM ammonium citrate, pH 7.0). SARS-CoV 3CLpro complex with compound **5**: Berkeley screen (Rigaku Reagents) condition B1 (30% [wt/vol] PEG 3350, 100 mM Tris, pH 8.5, 400 mM sodium chloride). SARS-CoV-2 3CLpro complex with compound **2**: Index HT screen condition G8 (25% [wt/vol] PEG 3350, 100 mM Hepes, pH 7.5, 200 mM ammonium acetate). SARS-CoV-2 3CLpro complex with compound **5**: Index HT condition D11 (28% PEG 2000 MME, 100 mM Bis-Tris, pH 6.5). Samples were transferred to a fresh drop composed of 80% crystallization solution and 20% (vol/vol) PEG 200 and stored in liquid nitrogen. All X-ray diffraction data were collected using a Dectris Eiger2  $\times$  9M pixel array detector at the Advanced Photon Source IMCA-CAT beamline 17-ID except for the data for the SARS-CoV-2 3CLpro complex with compound **5**, which were collected at the National Synchrotron Light Source II (NSLS-II) AMX beamline 17-ID-1.

**Structure Solution and Refinement.** Intensities were integrated using XDS via Autoproc (52) and the Laue class analysis and data scaling were performed with Aimless (53). Structure solution was conducted by molecular replacement with Phaser (54) using previously determined structures of SARS-CoV 3CLpro (PDB ID code 6W2A) and SARS-CoV-2 3CLpro (PDB ID code 6XMK) as the search models (6). Structure refinement and manual model building were conducted with Phenix (55) and Coot (56), respectively. Disordered side chains were truncated to the point for which electron density could be observed. Structure validation was conducted with Molprobit (57), and figures were prepared using the CCP4MG package (58). Superpositions were performed using GESAMT (59). Crystallographic data are provided in *SI Appendix, Table S1*.

**Animal Care and Ethics Statement.** *In vivo* studies were performed in animal biosafety level 3 facilities at The University of Iowa. All experiments were conducted under protocols approved by the Institutional Animal Care and Use Committee at The University of Iowa according to guidelines set by the Association for the Assessment and Accreditation of Laboratory Animal Care and the US Department of Agriculture.

**Postinfection Treatment in a Mouse Model of SARS-CoV-2 Infection.** Compound **2** was examined for efficacy using 7- to 8-wk-old female K18-hACE2 mice infected with SARS-CoV-2 (18). In the first experiment, animals were divided

into two groups ( $n = 4$  for vehicle or  $n = 5$  for compound 2) and were lightly anesthetized with ketamine/xylazine prior to infection with  $50 \mu\text{L}$  of  $2 \times 10^3$  pfu SARS-CoV-2 (the 2019n-CoV/USA-WA1/2019 strain of SARS-CoV-2; accession number: MT985325.1) via intranasal inoculation. Compound 2 was formulated in 10% ethanol and 90% PEG400 and given to mice from 1 (24 h postinfection) to 10 dpi at  $100 \text{ mg}\cdot\text{kg}^{-1}\cdot\text{d}^{-1}$  (once per day) via intraperitoneal administration. Control mice received vehicle. Animals were weighed daily and monitored for 15 d. Animals were killed when an animal lost 30% of initial weight or at 15 dpi. In the second experiment, mice were divided into two groups ( $n = 4$  for vehicle or  $n = 6$  for compound 2) and infected with  $50 \mu\text{L}$  of  $5 \times 10^3$  pfu SARS-CoV-2 via intranasal inoculation. Compound 2 was given to mice from 1 (24 h postinfection) to 10 dpi at  $125 \text{ mg}\cdot\text{kg}^{-1}\cdot\text{d}^{-1}$  (once per day) via intraperitoneal administration. The third experiment was conducted simultaneously with the second one to determine virus titers and histopathology in the lungs of mice treated with vehicle or compound 2 ( $n = 3$  for virus titration and  $n = 1$  or 2 for histopathology for each group at each dpi). Animals were killed at 2 or 5 dpi, and lungs and brains were removed aseptically and dissociated with a manual homogenizer in  $1\times$  phosphate-buffered saline. The homogenized lung and brain tissues were briefly centrifuged, and supernatants were removed. Virus titration was conducted in Vero E6 cells against SARS-CoV-2 (18). For histopathology, lungs and brains were fixed with 10% formalin, and hematoxylin and eosin-stained tissues were examined by a veterinary pathologist using the postexamination method of masking (18). Lung tissues were evaluated for edema (0 to 4) using distribution-based ordinal scoring: 0, none; 1, <25% of field; 2, 26 to 50% of field; 3, 51 to 75% of field; and 4, >75% of field. Perivascular inflammation was evaluated by severity-based ordinal scoring: 0, none; 1, scant solitary cellular infiltrates that do not form aggregates; 2, mild infiltrates that form loose cuff (~1 cell thickness) around vessel; 3, infiltrates form a distinct perivascular aggregate approximately two to four cells thick; and 4, large perivascular aggregates (more than four cells thick) that extend to compress adjacent tissues.

1. S. Perlman, P. S. Masters, "Coronaviridae: The viruses and their replication" in *Fields Virology: Emerging Viruses*, M. Howley, D. M. Knipe, S. Whelan, Eds. (Lippincott Williams & Wilkins, Philadelphia, 2020), chap. 10.
2. F. Wu *et al.*, A new coronavirus associated with human respiratory disease in China. *Nature* **579**, 265–269 (2020).
3. NIH, *COVID-19 Treatment Guidelines* (NIH, 2021).
4. J. N. Gustine, D. Jones, Immunopathology of hyperinflammation in COVID-19. *Am. J. Pathol.* **191**, 4–17 (2021).
5. K. Vanduyck *et al.*, ALG-097111, a potent and selective SARS-CoV-2 3-chymotrypsin-like cysteine protease inhibitor exhibits in vivo efficacy in a Syrian Hamster model. *Biochem. Biophys. Res. Commun.* **555**, 134–139 (2021).
6. A. D. Rathnayake *et al.*, 3C-like protease inhibitors block coronavirus replication in vitro and improve survival in MERS-CoV-infected mice. *Sci. Transl. Med.* **12**, eabc5332 (2020).
7. C. Joaquín Cáceres *et al.*, Efficacy of GC-376 against SARS-CoV-2 virus infection in the K18 hACE2 transgenic mouse model. *bioRxiv* [Preprint] (2021). <https://doi.org/10.1101/2021.01.27.428428> (Accessed 31 March 2021).
8. S. Dotolo, A. Marabotti, A. Facchini, R. Tagliaferri, A review on drug repurposing applicable to COVID-19. *Brief. Bioinform.* **22**, 726–741 (2021).
9. Y. Kim *et al.*, Broad-spectrum antivirals against 3C or 3C-like proteases of picornaviruses, noroviruses, and coronaviruses. *J. Virol.* **86**, 11754–11762 (2012).
10. A. C. Galasiti Kankanamalage *et al.*, Structure-guided design of potent and permeable inhibitors of MERS coronavirus 3CL protease that utilize a piperidine moiety as a novel design element. *Eur. J. Med. Chem.* **150**, 334–346 (2018).
11. Y. Kim *et al.*, Reversal of the progression of fatal coronavirus infection in cats by a broad-spectrum coronavirus protease inhibitor. *PLoS Pathog.* **12**, e1005531 (2016).
12. N. C. Pedersen *et al.*, Efficacy of a 3C-like protease inhibitor in treating various forms of acquired feline infectious peritonitis. *J. Feline Med. Surg.* **20**, 378–392 (2018).
13. L. Bao *et al.*, The pathogenicity of SARS-CoV-2 in hACE2 transgenic mice. *Nature* **583**, 830–833 (2020).
14. K. H. Dinno 3rd *et al.*, A mouse-adapted model of SARS-CoV-2 to test COVID-19 countermeasures. *Nature* **586**, 560–566 (2020).
15. S. H. Sun *et al.*, A mouse model of SARS-CoV-2 infection and pathogenesis. *Cell Host Microbe* **28**, 124–133.e4 (2020).
16. R. D. Jiang *et al.*, Pathogenesis of SARS-CoV-2 in transgenic mice expressing human angiotensin-converting enzyme 2. *Cell* **182**, 50–58.e8 (2020).
17. E. S. Winkler *et al.*, SARS-CoV-2 infection of human ACE2-transgenic mice causes severe lung inflammation and impaired function. *Nat. Immunol.* **21**, 1327–1335 (2020).
18. J. Zheng *et al.*, COVID-19 treatments and pathogenesis including anosmia in K18-hACE2 mice. *Nature* **589**, 603–607 (2020).
19. F. S. Oladunni *et al.*, Lethality of SARS-CoV-2 infection in K18 human angiotensin-converting enzyme 2 transgenic mice. *Nat. Commun.* **11**, 6122 (2020).
20. M. Taquet, J. R. Geddes, M. Husain, S. Luciano, P. J. Harrison, 6-month neurological and psychiatric outcomes in 236 379 survivors of COVID-19: A retrospective cohort study using electronic health records. *Lancet Psychiatry* **8**, 416–427 (2021).
21. P. B. McCray Jr *et al.*, Lethal infection of K18-hACE2 mice infected with severe acute respiratory syndrome coronavirus. *J. Virol.* **81**, 813–821 (2007).
22. W. Vuong *et al.*, Feline coronavirus drug inhibits the main protease of SARS-CoV-2 and blocks virus replication. *Nat. Commun.* **11**, 4282 (2020).
23. C. De Savi, D. L. Hughes, L. Kvaerno, Quest for a COVID-19 cure by repurposing small-molecule drugs: Mechanism of action, clinical development, synthesis at scale, and outlook for supply. *Org. Process Res. Dev.* **24**, 940–976 (2020).
24. S. Fan *et al.*, Research progress on repositioning drugs and specific therapeutic drugs for SARS-CoV-2. *Future Med. Chem.* **12**, 1565–1578 (2020).
25. B. N. Williamson *et al.*, Clinical benefit of remdesivir in rhesus macaques infected with SARS-CoV-2. *Nature* **585**, 273–276 (2020).
26. Y. Li *et al.*, Remdesivir metabolite GS-441524 effectively inhibits SARS-CoV-2 infection in mice models. *bioRxiv* [Preprint] (2020). <https://doi.org/10.1101/2020.10.26.353300> (Accessed 31 March 2021).
27. A. J. Pruijssers *et al.*, Remdesivir inhibits SARS-CoV-2 in human lung cells and chimeric SARS-CoV expressing the SARS-CoV-2 RNA polymerase in mice. *Cell Rep.* **32**, 107940 (2020).
28. Y. Wang *et al.*, Remdesivir in adults with severe COVID-19: A randomised, double-blind, placebo-controlled, multicentre trial. *Lancet* **395**, 1569–1578 (2020).
29. W. H. O. S. T. Consortium *et al.*, Repurposed antiviral drugs for covid-19—Interim WHO solidarity trial results. *N. Engl. J. Med.* **384**, 497–511 (2020).
30. J. H. Beigel *et al.*, Remdesivir for the treatment of covid-19—Final report. *N. Engl. J. Med.* **383**, 1813–1826 (2020).
31. A. C. Kalil *et al.*, Baricitinib plus remdesivir for hospitalized adults with covid-19. *N. Engl. J. Med.* **384**, 795–807 (2020).
32. D. E. Gordon *et al.*, A SARS-CoV-2-human protein-protein interaction map reveals drug targets and potential drug-repurposing. *bioRxiv* [Preprint] (2020). <https://doi.org/10.1101/2020.03.22.002386> (Accessed 31 March 2021).
33. H. Zhou *et al.*, Potential therapeutic targets and promising drugs for combating SARS-CoV-2. *Br. J. Pharmacol.* **177**, 3147–3161 (2020).
34. S. Joshi, M. Joshi, M. S. Degani, Tackling SARS-CoV-2: Proposed targets and repurposed drugs. *Future Med. Chem.* **12**, 1579–1601 (2020).
35. W. Dai *et al.*, Structure-based design of antiviral drug candidates targeting the SARS-CoV-2 main protease. *Science* **368**, 1331–1335 (2020).
36. R. L. Hoffman *et al.*, Discovery of ketone-based covalent inhibitors of coronavirus 3CL proteases for the potential therapeutic treatment of COVID-19. *J. Med. Chem.* **63**, 12725–12747 (2020).
37. T. P. Sheahan *et al.*, An orally bioavailable broad-spectrum antiviral inhibits SARS-CoV-2 in human airway epithelial cell cultures and multiple coronaviruses in mice. *Sci. Transl. Med.* **12**, eabb5883 (2020).
38. L. Fu *et al.*, Both Boceprevir and GC376 efficaciously inhibit SARS-CoV-2 by targeting its main protease. *Nat. Commun.* **11**, 4417 (2020).
39. C. Ma *et al.*, Boceprevir, GC-376, and calpain inhibitors II, XII inhibit SARS-CoV-2 viral replication by targeting the viral main protease. *Cell Res.* **30**, 678–692 (2020).
40. Y. Shi *et al.*, The preclinical inhibitor GS441524 in combination with GC376 efficaciously inhibited the proliferation of SARS-CoV-2 in the mouse respiratory tract. *Emerg. Microbes Infect.* **10**, 481–492 (2021).
41. M. de Vries *et al.*, A comparative analysis of SARS-CoV-2 antivirals characterizes 3CL<sup>pro</sup> inhibitor PF-00835231 as a potential new treatment for COVID-19. *J. Virol.*, 10.1128/JVI.01819-20 (2021).

#### Dampalla *et al.*

Postinfection treatment with a protease inhibitor increases survival of mice with a fatal SARS-CoV-2 infection

42. X. He *et al.*, Generation of SARS-CoV-2 reporter replicon for high-throughput antiviral screening and testing. *Proc. Natl. Acad. Sci. U.S.A.* **118**, e2025866118 (2021).
43. J. Qiao *et al.*, SARS-CoV-2 M<sup>pro</sup> inhibitors with antiviral activity in a transgenic mouse model. *Science* **371**, 1374–1378 (2021).
44. T. Pirali, M. Serafini, S. Cargini, A. A. Genazzani, Applications of deuterium in medicinal chemistry. *J. Med. Chem.* **62**, 5276–5297 (2019).
45. Y. C. Wang *et al.*, Structural basis of SARS-CoV-2 main protease inhibition by a broad-spectrum anti-coronaviral drug. *Am. J. Cancer Res.* **10**, 2535–2545 (2020).
46. Y. Kim *et al.*, Broad-spectrum inhibitors against 3C-like proteases of feline coronaviruses and feline caliciviruses. *J. Virol.* **89**, 4942–4950 (2015).
47. A. C. Galasiti Kankanamalage *et al.*, Structure-guided design and optimization of dipeptidyl inhibitors of norovirus 3CL protease. Structure-activity relationships and biochemical, X-ray crystallographic, cell-based, and in vivo studies. *J. Med. Chem.* **58**, 3144–3155 (2015).
48. A. C. Galasiti Kankanamalage *et al.*, Structure-based exploration and exploitation of the S<sub>4</sub> subsite of norovirus 3CL protease in the design of potent and permeable inhibitors. *Eur. J. Med. Chem.* **126**, 502–516 (2017).
49. A. C. Galasiti Kankanamalage *et al.*, Design, synthesis, and evaluation of novel prodrugs of transition state inhibitors of norovirus 3CL protease. *J. Med. Chem.* **60**, 6239–6248 (2017).
50. P. S. Dragovich *et al.*, Structure-based design, synthesis, and biological evaluation of irreversible human rhinovirus 3C protease inhibitors. 4. Incorporation of P1 lactam moieties as L-glutamine replacements. *J. Med. Chem.* **42**, 1213–1224 (1999).
51. D. P. Kjell, B. J. Slattery, M. J. Semo, A novel, nonaqueous method for regeneration of aldehydes from bisulfite adducts. *J. Org. Chem.* **64**, 5722–5724 (1999).
52. C. Vonrhein *et al.*, Data processing and analysis with the autoPROC toolbox. *Acta Crystallogr. D Biol. Crystallogr.* **67**, 293–302 (2011).
53. P. R. Evans, An introduction to data reduction: Space-group determination, scaling and intensity statistics. *Acta Crystallogr. D Biol. Crystallogr.* **67**, 282–292 (2011).
54. A. J. McCoy *et al.*, Phaser crystallographic software. *J. Appl. Cryst.* **40**, 658–674 (2007).
55. P. V. Afonine *et al.*, Towards automated crystallographic structure refinement with phenix.refine. *Acta Crystallogr. D Biol. Crystallogr.* **68**, 352–367 (2012).
56. P. Emsley, B. Lohkamp, W. G. Scott, K. Cowtan, Features and development of Coot. *Acta Crystallogr. D Biol. Crystallogr.* **66**, 486–501 (2010).
57. V. B. Chen *et al.*, MolProbity: All-atom structure validation for macromolecular crystallography. *Acta Crystallogr. D Biol. Crystallogr.* **66**, 12–21 (2010).
58. L. Potterton *et al.*, Developments in the CCP4 molecular-graphics project. *Acta Crystallogr. D Biol. Crystallogr.* **60**, 2288–2294 (2004).
59. E. Krissinel, Enhanced fold recognition using efficient short fragment clustering. *J. Mol. Biochem.* **1**, 76–85 (2012).